Advanced Functional Materials

ADVANCED FUNCTIONAL MATERIALS
www.afm-journal.de

RESEARCH ARTICLE OPEN ACCESS

Interlayer Expansion of Bulk MoS_2 via Top-Down Organic Pillaring Enables Tunable Li^+ Intercalation and Controlled Solvent Co-Intercalation

Jaehoon Choi[1,2] | Pakornrum Tulaphon[1,2] | Franz Jacobi[3] | Kyeonghyeon Nam[4] | Jameela Karol[1,2,5] | Mete B. Durukan[1,2] | Christoph Scheurer[4,6] | Desirée Leistenschneider[3,7] | Simon Fleischmann[1,2,5]

[1]Helmholtz Institute Ulm (HIU), Ulm, Germany | [2]Karlsruhe Institute of Technology (KIT), Karlsruhe, Germany | [3]Institute for Technical and Environmental Chemistry, Friedrich-Schiller University Jena, Jena, Germany | [4]Fritz Haber Institute of the Max Planck Society, Berlin, Germany | [5]CELEST Green Energy Lab Ulm, Ulm University, Ulm, Germany | [6]IET-1, Forschungszentrum Jülich, Jülich, Germany | [7]Center For Energy and Environmental Chemistry (CEEC) Jena, Friedrich-Schiller University Jena, Jena, Germany

Correspondence: Simon Fleischmann (simon.fleischmann@kit.edu)

Received: 19 March 2026 | **Revised:** 7 May 2026 | **Accepted:** 3 June 2026

Keywords: battery energy storage | electrochemical intercalation | lithium intercalation | molybdenum disulfide

ABSTRACT

Interlayer engineering is widely used to improve charge storage in layered transition metal dichalcogenides, yet most studies rely on nanosized materials where the effects of interlayer expansion and particle downsizing are intertwined. Here, molecular pillaring is translated to bulk molybdenum disulfide (MoS_2) using a top-down strategy. Chemical pre-reduction with butyllithium enables exfoliation and restacking in the presence of hexanediammonium (HDA) molecules, forming a pillared MoS_2-HDA structure with an expanded interlayer spacing of 0.98 nm while preserving the bulk particle morphology and specific surface area. Electrochemical analysis reveals that improved rate capability primarily originates from the chemical activation associated with the pre-reduction step rather than from interlayer expansion itself. Operando X-ray diffraction and electrochemical dilatometry show that bulk MoS_2 undergoes solvent co-intercalation in diglyme electrolyte, leading to pronounced lattice expansion and electrode swelling. In contrast, pillared MoS_2-HDA suppresses solvent co-intercalation despite its larger interlayer spacing, demonstrating that interlayer expansion alone does not dictate solvent co-intercalation in layered electrodes.

1 | Introduction

Layered transition-metal dichalcogenides (TMDs) like molybdenum disulfide (MoS_2) are classical host materials for ion intercalation owing to their highly accessible and tunable interlayer galleries. Early work established that the interlayer space of MoS_2 can accommodate foreign species. Seminal studies by Divigalpitiya et al. demonstrated so-called "organic inclusion compounds" based on restacked MoS_2 with various confined molecules, while Kanatzidis and co-workers introduced the concept of pillared layered chalcogenides, in which confined clusters act as structural spacers that open up the host lattice [1, 2]. These studies provided the conceptual basis for interlayer engineering in MoS_2.

In the past decade, this concept has been extensively revisited in the context of electrochemical energy storage. Bottom-up hydrothermal and solvothermal syntheses have enabled nanosized, interlayer-expanded MoS_2 that exhibit strongly enhanced rate capability and pseudocapacitive properties for the electrochemical Li^+ and Na^+ intercalation reactions [3, 4]. In these studies, interlayer expansion has been achieved by incorporating

---

organic molecules or polymers during synthesis, demonstrating that such a materials design approach can reduce solid-state diffusion barriers and/or increase ion storage capacity. Recently, we demonstrated that controlled interlayer expansion of MoS_2 can be achieved through organic pillar strategies during hydrothermal synthesis, using diamines and dithiols as molecular interlayer pillars [5, 6]. While these studies established clear structure-property relationships and tunable pillar-host interactions, they were inherently limited to nanoscale, bottom-up synthesized materials, where the effects of interlayer expansion and nanosizing are simultaneously present. While nanosized MoS_2 offers short diffusion lengths and high surface area [7, 8], it suffers from low bulk density [9]. The nanosized particles can also limit processability and present challenges in scaling, electrode fabrication, and recycling [10–12]. As a result, there is an urgent need to investigate whether the improved electrochemical performance commonly attributed to interlayer expansion can also be translated to bulk-sized materials.

From a practical perspective, commercially available bulk MoS_2 offers decisive advantages over nanosized MoS_2 obtained through bottom-up approaches, including higher bulk/tap density and a more straightforward integration into electrodes. Yet, systematic studies that translate organic pillaring strategies to bulk-sized MoS_2 are largely missing.

Here, we extend the materials design strategy of interlayer expansion through organic pillaring to bulk-sized MoS_2 using a top-down approach. Chemical pre-reduction of commercially available MoS_2-bulk with butyllithium yields lithiated Li_xMoS_2, which undergoes exfoliation upon exposure to aqueous media. In the presence of hexanediammonium (HDA), the positively charged diammonium species interact with the electron-rich MoS_2 layers with polar sulfide surfaces, leading to restacking with confined organic pillars within the interlayer galleries. This process yields a pillared MoS_2-HDA structure with an expansion in interlayer spacing from 0.62 to 0.98 nm while preserving the macroscopic particle morphology and specific surface area of the bulk material. Because chemical lithiation itself can induce partial exfoliation and a 2H-to-1T phase transformation, which are known to influence electrochemical behavior [13–15], a control sample subjected to the same pre-reduction and restacking procedure without HDA is investigated in parallel. Electrochemical measurements reveal that the improved rate capability of the modified MoS_2 materials is primarily associated with chemical activation induced by the pre-reduction step, rather than with interlayer expansion alone.

At the same time, recent work has demonstrated that ions can circumvent the desolvation step at the electrochemical interface and intercalate into the layered host material together with parts or the entirety of their solvation shell—a process called solvent co-intercalation [16, 17]. It was demonstrated that, particularly, the electrolyte solvation environment can strongly influence the resulting ion storage mechanism in TMD electrodes [18, 19], making the choice of electrolyte solvent of interest. Here, we find that bulk MoS_2 exhibits conventional Li^+ intercalation in carbonate-based electrolyte, while diglyme-based electrolyte can induce a transition to a solvent co-intercalation process. Importantly, pillared MoS_2-HDA suppresses solvent co-intercalation despite its larger interlayer spacing, demonstrating that increased interlayer spacing alone does not enable solvent co-intercalation in bulk MoS_2.

2 | Experimental

2.1 | Material Synthesis

For the preparation of chemically pre-lithiated, exfoliated, and partially restacked, and HDA-functionalized MoS_2, 1 g of commercial MoS_2 powder (Sigma–Aldrich, <2 µm, 98% purity) was chemically lithiated using n-butyllithium (*n*-BuLi, 1.6 M in hexane, Fisher Scientific). All procedures involving *n*-BuLi were carried out inside an Ar-filled glovebox (O_2, $H_2O < 0.5$ ppm). The MoS_2 powder was dispersed in 25 mL of hexane in a glass vial using magnetic stirring (500 rpm). Subsequently, 4.25 mL of *n*-BuLi solution (1.6 M in hexane, corresponding to ca. 1.1 Li per MoS_2) was added under continuous stirring. The suspension was maintained at 50°C for 48 h inside the glovebox. Hexane and *n*-Buli solution were withdrawn from septum sealed reagent bottles using a syringe and directly added to the reaction vial under inert conditions.

After the reaction, the vial was tightly sealed before being transferred to a fume hood. The resulting lithiated MoS_2 (Li_xMoS_2) was collected by vacuum filtration using a 0.22 µm hydrophilic polytetrafluoroethylene (PTFE) membrane (Millipore), washed thoroughly with hexane, and dried under vacuum to remove residual solvent. For exfoliation, 200 mg of dried Li_xMoS_2 was dispersed in 100 mL of deionized (DI) water and stirred for 30 min, followed by 10 min of bath sonication. The resulting suspension was filtered, rinsed with DI water and ethanol, and then redispersed in 30 mL of DI water by hand-shaking and an additional 5 min of bath sonication. The suspension was frozen in liquid nitrogen and subsequently freeze-dried (Alpha 3–4 LSCbasic, Martin Christ) for 72 h to yield exfoliated and partially restacked MoS_2 powder, labelled MoS_2-restack.

For the pillaring of 1,6-hexanediamine (HDA) molecules into MoS_2 layers, 25 µL of 60 wt.% aqueous HDA solution (Fisher Scientific) was added to 100 mL of deionized (DI) water. Subsequently, 200 mg of Li_xMoS_2 powder was dispersed in this solution, corresponding to a 1:0.1 molar ratio between MoS_2 and HDA, followed by 5 min of bath sonication and continuous stirring for 48 h at ambient temperature.

After the reaction, the HDA-functionalized MoS_2 samples were vacuum-filtered and rinsed with DI water and ethanol to remove residual species. The resulting slurry was prepared using the same redispersion procedure as the exfoliated MoS_2 sample. The suspension was subsequently frozen and freeze-dried under the same conditions to obtain MoS_2-HDA powders.

2.2 | Material Characterization

The crystalline structure of the synthesized powders was analyzed by X-ray diffraction (XRD) in Bragg–Brentano geometry using a Bruker D8 Advance diffractometer with Cu Kα radiation source ($\lambda = 1.5406$ Å) and a LYNXEYE XE-T detector with a step size of 0.02° and a dwell time of 1 s.

Raman spectra were recorded to evaluate phase and structural changes using a Renishaw InVia confocal Raman microscope equipped with a 532 nm excitation laser. To prevent thermal degradation of the samples, the laser power was restricted to 0.5 mW, and spectra were averaged from at least three distinct sample locations.

Fourier transform infrared spectroscopy (FTIR) measurements were performed using a Spectrum Two FTIR spectrometer (PerkinElmer) at resolutions of 8 and 16 cm^{-1} over 20 scans, covering the spectral range from 400 to 4000 cm^{-1}.

Thermal stability and organic content were quantified via thermogravimetric analysis (TGA) using a Netzsch TG 209 F1 Libra analyzer. Samples were heated at a rate of 5 K min^{-1} under a flow of oxygen and nitrogen (1:1 ratio, 20 mL min^{-1}).

Nitrogen adsorption-desorption isotherms were measured at 77 K using a volumetric gas sorption analyzer (Quadrasorb, Quantachrome, Anton Paar). Prior to the measurement, samples were degassed for 24 h at 100°C under vacuum (~0.02 mbar). The specific surface area was calculated using the Brunauer–Emmett–Teller (BET) method within a relative pressure range of $0.05 < p/p_0 < 0.2$ using ASiQwin software, Quantachrome.

Particle morphology was analyzed using a field emission scanning electron microscope (SEM, Zeiss Crossbeam x340) at an accelerating voltage of 5 kV.

Surface chemistry and oxidation states were probed by X-ray photoelectron spectroscopy (XPS) using a SPECS UHV system (FOCUS 500) with a monochromatic Al Kα source ($h\nu$ = 1486.6 eV) and a PHOIBOS 150 hemispherical analyzer with a 2D DLD detector (Surface Concept). High-resolution spectra were recorded at a pass energy of 30 eV with a 0.1 eV step size. Surface charging was compensated during XPS acquisition using an electron flood gun operated at 5 eV and 2.5 μA. Data analysis was performed using CasaXPS software, applying a Shirley background and GL(30) line shape, with binding energies calibrated to the C–C/C–H sp^3 reference at 284.8 eV.

2.3 | Electrode Preparation and Electrochemical Characterization

2.3.1 | Standard Coin Cell Electrode Fabrication

A slurry was prepared by mixing the active material (bulk or HDA-functionalized MoS_2), carbon black (CB, Imerys, C-NERGY Super C65), and polyvinylidene difluoride (PVDF, Solvay, Solef 6020) in a weight ratio of 8:1:1. First, the MoS_2-based powders and CB were homogeneously ground together using a pestle and mortar. This dry mixture was then transferred to a container, and a 2 wt.% PVDF solution in N-methyl-2-pyrrolidone (NMP, Sigma–Aldrich, 99.5%) was added. The resulting slurry was homogenized using a speed mixer (ARE-250, Thinky) at 1000 rpm for 10 min.

The slurry was coated onto carbon-coated battery-grade aluminum foil (20 μm, Wellcos) using a doctor blade (wet film thickness: 90 μm) and dried overnight at 80°C to remove the NMP solvent. Circular electrodes (12 mm diameter) were punched from the dried film and transferred to an argon-filled glovebox. The mass loading of the MoS_2 electrodes was maintained between 0.8 and 1.2 mg cm^{-2}. We purposefully employed electrodes with relatively low mass loadings to study intrinsic materials properties and minimize limitations imposed by the electrode architecture. Mass normalizations for electrochemical metrics refer to the active material, that is, MoS_2 and pillars combined, but omitting the mass of the inactive PVDF binder and CB additive.

2.3.2 | Electrodes for Operando Experiments

A separate electrode formulation was prepared for operando XRD and electrochemical dilatometry (ECD) experiments, consisting of 60 wt.% active material, 30 wt.% CB, 10 wt.% PVDF dissolved in NMP. The mixture was stirred overnight on a stirring plate at room temperature to ensure homogeneous mixing. This prevented large polarization in (non-ideal) operando cells.

For operando XRD, the slurry was drop-casted onto a Ti mesh current collector and dried overnight in an oven at 80°C. The dried electrodes were subsequently pressed under 1 ton using a hydraulic press (Spcac).

For ECD, the slurry was cast directly onto the stainless steel plunger of the dilatometer (which served as the current collector) and dried overnight at 80°C. A final pressing step of 2 tons was applied to the dried electrode using the hydraulic press.

2.3.3 | Cell Assembly and Electrochemical Testing

2032-type coin cells (Hohsen) were assembled in an argon-filled glovebox (MBraun; O_2, H_2O < 0.5 ppm). Metallic lithium discs (14 mm diameter, Honjo) served as the negative electrodes. The cell components included a 1 mm thick stainless steel spacer, a stainless steel spring, and a glass microfiber separator (Whatman grade GF/A).

Two distinct electrolytes were prepared for this study. The carbonate-based electrolyte consisted of 1 M Lithium bis(trifluoromethanesulfonyl)imide (LiTFSI, Sigma–Aldrich, 99.95%) salt dissolved in a 1:1 volumetric ratio of ethylene carbonate (EC, Sigma–Aldrich, ≥99%) and dimethyl carbonate (DMC, Fisher Scientific, 99 + %). The ether-based electrolyte was prepared by dissolving 1 M LiTFSI in diethylene glycol dimethyl ether (2G, Sigma–Aldrich, 99.5%). LiTFSI was selected as the conducting salt to ensure compatibility with both carbonate-based (EC/DMC) and ether-based (2G) electrolytes. All electrolyte mixtures were prepared and stirred overnight in the glovebox (O_2, H_2O < 0.1 ppm). Each coin cell was filled with 120 μL of either the carbonate- or ether-based electrolyte.

Electrochemical tests were performed using potentiostats (Bio-Logic VMP3-e and VMP300). Cyclic voltammetry (CV) and galvanostatic charge/discharge (GCD) tests were conducted within a potential window of 1.0 to 3.0 V versus Li^+/Li at a controlled temperature chamber at 20°C (Binder). Long-term cycling performance was evaluated at a constant specific current of 0.1 A g^{-1}.

For operando XRD experiments, a customized operando 2032-coin cell design with central windows was utilized. These cells featured 4 mm diameter central holes in both the negative and positive caps, which were sealed with Kapton tape, and a spacer with a 4 mm diameter central hole. The overall procedure for the XRD cells matched that of the standard coin cells, but the electrolyte volume was increased to ca. 200 µL. The fabricated cells were mounted in a STADI-p diffractometer (STOE) equipped with a coin cell holder, utilizing a silver X-ray source (Ag K_α = 0.5594074 Å) for the experiment.

For ECD measurements, a high-resolution electrochemical dilatometer (ECD-4-nano, EL-CELL) was assembled in the Ar-filled glovebox. Li metal (8 mm diameter) served as the counter electrode, with a GF/A separator (10 mm diameter) positioned between the Li electrode and a glass T-Frit. Approximately 300–350 µL of electrolyte was injected onto the T-Frit, and the working electrode, coated directly onto the plunger, was placed on top of the T-Frit. The cell was sealed using the screw cap unit with a membrane to ensure airtightness and electrical contact. Following transfer from the glovebox, the sensor head was attached, and the cell was connected to a docking station (PAT-Stand-1, EL-CELL) housed in a temperature-controlled chamber at 22°C and connected to a potentiostat (BioLogic VMP3).

2.4 | Computational Details

For the isolated diglyme (2G) and Li^+-2G clusters, initial geometry optimization was performed using density functional theory (DFT) in ORCA [20] with the B3LYP functional [21, 22]. The pre-optimized cluster structures were then used as input for Quantum Espresso simulations of 2G, Li^+-(2G), and Li^+-$(2G)_2$ intercalated 1T-MoS_2. The 1T-MoS_2 host structure was constructed based on its primitive unit cell (octahedral coordination, trigonal symmetry), with lattice parameters of $a = 3.193$ Å and $c = 6.014$ Å. All QE calculations employed orthogonal norm-conserving Vanderbilt (ONCV) pseudopotentials from the PseudoDojo library [23], with the Perdew–Burke–Ernzerhof (PBE) exchange–correlation functional [24]. Long-range dispersion interactions were treated using Grimme D3 van der Waals correction with zero damping (PBE+D3) [25], applied throughout all QE calculations. Structure optimization was carried out in a $(4 \times 4 \times 1)$ supercell, where Mo atoms were kept fixed within the layer plane to isolate interlayer expansion effects induced by the intercalated species, while minimizing contribution from intralayer distortions. The interlayer distances and guest species were fully relaxed. The Brillouin zone was sampled using Γ-centered k-point grids generated from a uniform reciprocal-space spacing of 0.05 $Å^{-1}$ (equivalent to a $2 \times 2 \times 4$ grid for the $4 \times 4 \times 1$ MoS_2 supercell). Structural relaxation convergence thresholds were set to 10^{-6} Ry for total energy and 10^{-4} Ry/bohr (or tighter) for forces. Then, the XRD spectra of the DFT-simulated MoS_2 variants were calculated via VESTA with Ag $K\alpha_1$ wavelength of 0.5594 Å [26]. Here, to examine the structural influence of trapped solvated Li species on the host interlayer spacing, a neutral Li-2G complex was employed as a simplified model in the periodic calculations, focusing on the steric and local coordination effects governing interlayer expansion.

3 | Results and Discussion

3.1 | Structural Characterization of MoS_2-Based Materials

The goal of this work is to extend the interlayer expansion strategy via molecular pillaring with hexanediammonium (HDA) from previously described bottom-up grown nanomaterials toward top-down pillaring of bulk MoS_2. We employ commercially available bulk MoS_2 as the starting material and use a chemical pre-reduction step with butyllithium to obtain Li_xMoS_2. Subsequent exposure to an aqueous solution of HDA leads to the formation of MoS_2-HDA. To disentangle the respective roles of chemical pre-reduction and interlayer expansion for the subsequent electrochemical tests, Li_xMoS_2 is also exposed to water without HDA molecules, to obtain exfoliated and partially restacked MoS_2 as a control sample. The synthesis procedure is outlined schematically in Figure 1.

The morphological evolution of the materials was examined by scanning electron microscopy (SEM). Commercial, bulk MoS_2 consists of irregularly shaped, platelet-like particles with well-defined flat facets, consistent with the layered crystal structure of MoS_2. The particles form micrometer-sized aggregates composed of stacked lamellae with clearly visible layered edges (Figure 2A). After chemical pre-reduction, exfoliation in water, and partial restacking, the control sample MoS_2-restack exhibits compact platelet-like crystallites but displays a more disordered morphology composed of thinner sheets. The sample forms loosely packed aggregates with folded and partially delaminated layers, indicating a disruption of the original stacked lamellar structure after exfoliation and restacking (Figure 2B). The pillared MoS_2-HDA sample shows a morphology similar to bulk MoS_2, however, with a stacking that appears slightly looser and edges that indicate a partially separated lamellae structure (Figure 2C).

The crystal structure of the materials was then characterized by X-ray diffraction (XRD, Figure 2D). Commercial, bulk-MoS_2 exhibits the characteristic diffractogram of 2H-MoS_2, according to PDF card #01-071-9809, with an interlayer spacing of 0.62 nm, as visible from the diffraction peak at 14.4 °2θ corresponding to the 002 set of planes. After chemical lithiation with butyllithium, the interlayer spacing of Li_xMoS_2 increases to 1.13 nm, visible from a shift of the diffraction signal to 7.84 °2θ in agreement with previous reports [27]. This is indicative of Li^+ and hexane confined between the bulk MoS_2 layers, and the complete absence of the original 002 signal at 14.4° indicates extensive lithiation of the MoS_2 structure. The presence of a higher order (002) diffraction peak in Li_xMoS_2 confirms a well-defined periodic stacking along the c-axis, indicating a uniform interlayer spacing despite the significant expansion induced by chemical lithiation.

Upon immersion of Li_xMoS_2 in aqueous solution (both with and without HDA), the intercalated lithium reacts with water according to the well-known chemical exfoliation mechanism ($Li_xMoS_2 + xH_2O \rightarrow MoS_2\hat{}(\delta^-) + x\text{LiOH} + x/2\ H_2$) [28], generating MoS_2 sheets with negative partial charge that electrostatically repel each other and undergo exfoliation. Without the presence of HDA pillar molecules, the MoS_2 sheets (partially) restack and form again a crystalline MoS_2 structure with the characteristic

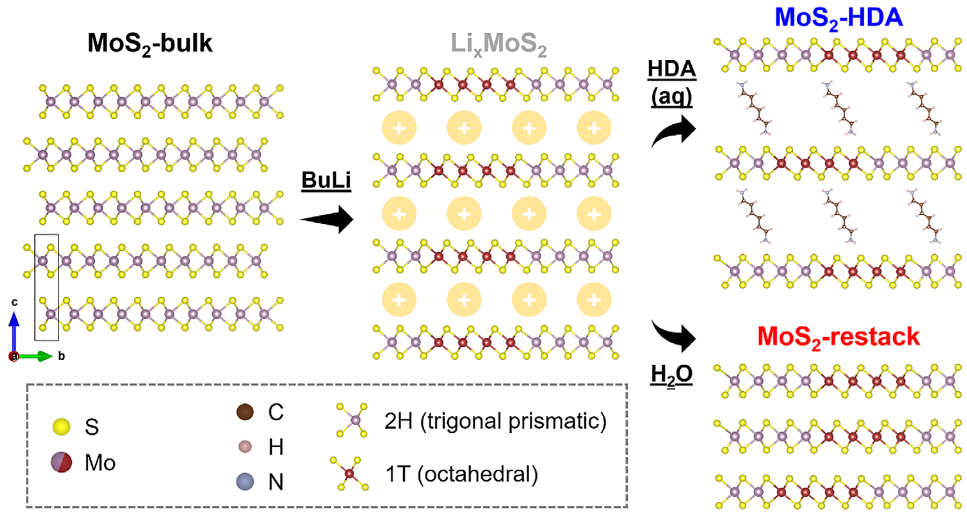

FIGURE 1 | Schematic synthesis procedure of pillaring MoS$_2$-bulk via a top-down approach involving chemical pre-reduction using butyllithium to form Li$_x$MoS$_2$ and subsequent immersion in an aqueous solution of HDA pillars, resulting in MoS$_2$-HDA. Immersion of Li$_x$MoS$_2$ in H$_2$O and subsequent filtration yields a partially restacked MoS$_2$ control sample. The depicted 1T/2H-ratio in Li$_x$MoS$_2$, MoS$_2$-restack, and MoS$_2$-HDA indicates their mixed phase character and is for illustrative purposes only.

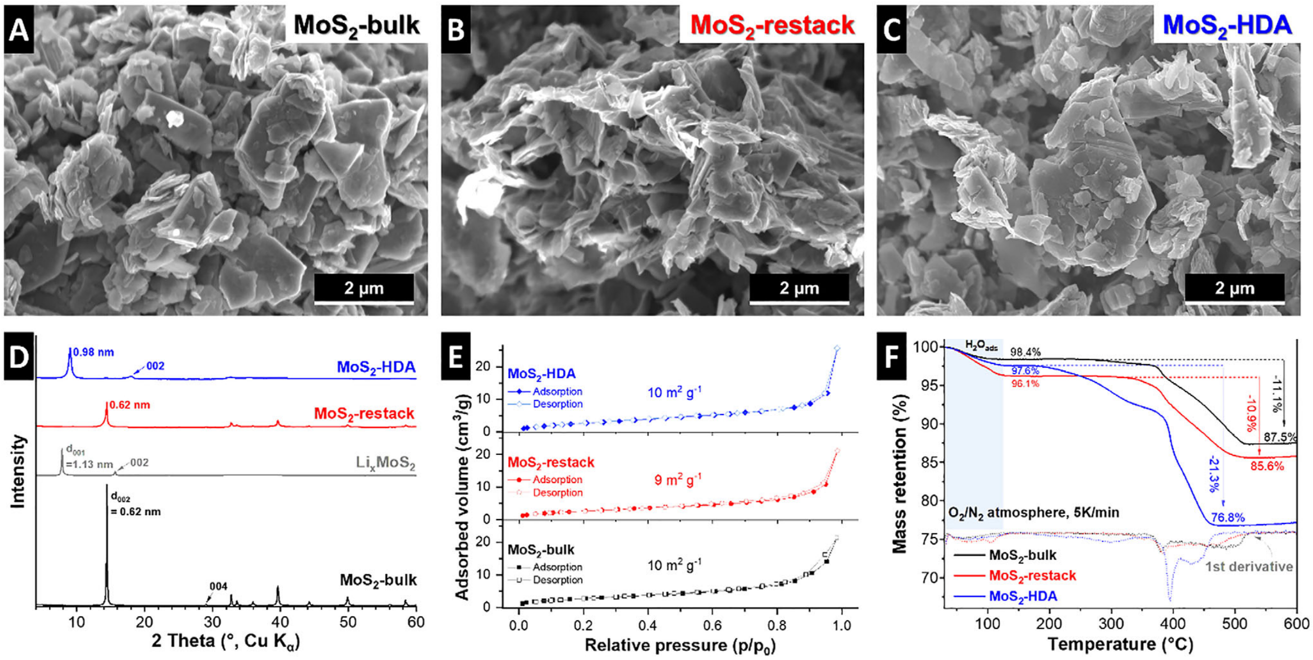

FIGURE 2 | Scanning electron micrographs of (A) MoS$_2$-bulk, (B) MoS$_2$-restack, and (C) MoS$_2$-HDA. (D) X-ray diffractograms, (E) nitrogen sorption isotherms, and (F) thermogravimetric analysis in O$_2$/N$_2$ atmosphere at a heating rate of 5 K min^{-1} for the three materials.

interlayer spacing at 0.62 nm visible from the diffraction peak at 14.4°, however, the lower intensity and broadening of the 002 signal of MoS$_2$-restack compared to bulk MoS$_2$ indicates a decreased stacking order in agreement with SEM observations.

When HDA is added to the aqueous solution (at a molar ratio corresponding to 0.1 HDA per MoS$_2$), a distinct change in the diffraction pattern is observed. The main diffraction signal is shifted to 9.04°, indicative of an interlayer spacing of 0.98 nm in MoS$_2$-HDA and the successful confinement of the cationic HDA molecules in the MoS$_2$ interlayer space. The same interlayer spacing was observed previously for HDA-pillared MoS$_2$ nanomaterials that were grown bottom-up during hydrothermal synthesis [6]. The presence of a higher-order (002) reflection further confirms preserved stacking periodicity in the expanded, pillared MoS$_2$-HDA. Note that MoS$_2$-HDA materials synthesized at higher HDA concentrations in the aqueous solution during pillaring (e.g., 0.5 or 1 HDA per MoS$_2$) exhibit the same interlayer spacing (Figure S1A).

Nitrogen sorption measurements were performed to evaluate the porosity and accessible surface area of the samples. The sorption isotherms of bulk MoS_2, MoS_2-restack, and MoS_2-HDA all exhibit high similarity (Figure 2E). They most closely resemble a type III shape according to the IUPAC technical report [29], indicative of their non-porous (or macroporous) structure. There are very small hysteresis loops noticeable for all samples that can best be classified as type H3, indicative of non-rigid aggregates of plate-like particles [29]. The Brunauer–Emmett–Teller (BET) specific surface areas of bulk, restacked, and HDA-pillared MoS_2 are all around 9–10 $m^2\ g^{-1}$, quantitatively confirming that the top-down pillaring approach was able to maintain the bulk character of the MoS_2 sample, while primarily alters the internal interlayer structure.

Thermogravimetric analysis (TGA) was employed to quantify the number of confined guests within the pillared MoS_2 interlayer space (Figure 2F). TGA profiles reveal two major mass-loss stages: (1) removal of adsorbed surface water up to ca. 130°C, and (2) conversion of MoS_2 to MoO_3 under oxidative atmosphere (via $2MoS_2 + 5O_2 \rightarrow 2MoO_3 + 4SO_2$) [30] and evaporation and/or combustion of organic HDA molecules, above ca. 200°C, where the latter two processes are partially overlapping. In stage 1, the mass loss of adsorbed surface water is 1.6 wt.% for bulk MoS_2, 2.4 wt.% for MoS_2-HDA, and 3.9 wt.% for MoS_2-restack, which indicates the highest area for water adsorption on the latter sample despite its comparable BET surface area relative to MoS_2-bulk and MoS_2-HDA. In stage 2, further heating of MoS_2-bulk and MoS_2-restack leads to an additional mass loss of around 11 wt.% (relative to the weight after H_2O loss), which is consistent with the theoretical value (10.1 wt.%) expected for the conversion of MoS_2 to MoO_3. MoS_2-HDA shows an additional mass loss of 21.3 wt.%, leading to an estimated content of ca. 0.20 HDA molecules per formula unit of MoS_2. A comparable composition is observed for MoS_2-HDA samples prepared with different HDA concentrations during synthesis (Figure S1B), indicating that the amount of confined HDA pillars in the MoS_2 interlayer space is largely independent of the precursor solution concentration under the applied synthesis conditions.

Raman spectroscopy is carried out to assess the phase composition and layer coupling of the MoS_2 host material. The Raman spectra of MoS_2-bulk and MoS_2-restack exhibit characteristic E^1_{2g} (in-plane) and A_{1g} (out-of-plane) modes at 384 and 409 cm^{-1}, respectively (Figure 3A) [31]. In comparison, the MoS_2-HDA spectrum shows both modes shifted to lower wavenumbers (redshift) to 381 and 407 cm^{-1}, respectively. This redshift is primarily attributed to the interlayer expansion induced by confined HDA pillars, which weakens the van der Waals coupling between adjacent layers and reduces the restoring force for lattice vibration [32]. While electrostatic interactions between the protonated ammonium groups ($R\text{-}NH_3^+$) and the MoS_2 layers are present, their specific contribution to the Raman shifts cannot be excluded. The observed redshift is primarily attributed to the expansion of the MoS_2 spacing, which weakens the van der Waals coupling between adjacent layers and reduces the restoring force for lattice vibration, while any additional contribution from electrostatic interactions cannot be distinguished from this structural effect. Additionally, the emergence of J_1 (156 cm^{-1}) and J_2 (226 cm^{-1}) modes in MoS_2-HDA (and to a lesser extent in MoS_2-restack) confirms the mixed 1T/2H-phase character of the material, resulting from the partial 2H-to-1T phase transformation induced during chemical pre-lithiation (Figure S2) [33]. These 1T-specific modes are absent in the MoS_2-bulk spectrum, which instead displays a strong E_g mode (287 cm^{-1}), indicating that MoS_2-bulk is in a purely semiconducting 2H-phase, while the modified samples coexist as mixed 2H/1T phases [34].

The Fourier transform infrared spectrum (FTIR, Figure 3B) of functionalized MoS_2-HDA reveals two C–H stretching modes at 2912 and 2850 cm^{-1}, confirming the presence of *n*-alkyl chains that originate from the HDA pillars and indicating successful incorporation between MoS_2 layers [6]. These peaks are absent in the spectrum of MoS_2-bulk.

X-ray photoelectron spectroscopy (XPS) reveals clear chemical changes in interlayer-expanded MoS_2 functionalized with HDA pillars. A distinct N 1s component at 401.9 eV (Figure 3C) is consistent with protonated amine/ammonium species ($R\text{-}NH_3^+$). We thus hypothesize that cationic ammonium groups electrostatically interact with the partially negatively charged outer sulfide layers of the MoS_2 host material [35, 36]. The Mo $3p_{3/2}$ peak shifts from 395.75 eV in bulk MoS_2 to 395.24 eV in MoS_2-HDA, and the Mo $3d_{5/2}$ peak from 229.86 to 229.41 eV (Figure S3), indicating a modification of the local electronic environment. This shift is likely influenced by both the presence of metallic 1T/1T' MoS_2, which exhibits lower binding energies compared to the 2H phase, and electrostatic interactions with confined HDA molecules, although these contributions cannot be clearly separated.

Chemical lithiation introduces additional electron density into the MoS_2 layers, which is expected to occupy delocalized states associated with the metallic 1T/1T' phase. In the presence of protonated ammonium groups ($R\text{-}NH_3^+$), this interaction can be understood as an electrostatic polarization of this delocalized electron density, rather than the formation of reduced Mo species. Charge neutrality is expected to be preserved through electrostatic compensation between the MoS_2 layers and the protonated ammonium groups, without implying localized charge transfer.

In addition to the dominant 2H-MoS_2 features, lower binding energy components in the Mo 3d and S 2p regions corresponding to metallic 1T-MoS_2 are primarily observed in MoS_2-HDA (Figure 3D), consistent with the Raman results and the 2H-to-1T phase transformation induced during chemical lithiation. Increased Mo^{6+} contributions in MoS_2-restack and MoS_2-HDA in the Mo 3p and Mo 3d regions, along with SO_x^{2-} (x = 3, 4) features at 168–170 eV in the S 2p region, indicating partial surface oxidation of MoS_2 during chemical processing.

These structural analyses confirm the successful preparation of three MoS_2-based materials with distinct interlayer architectures and phase compositions, providing a well-defined platform to investigate the influence of chemical activation and interlayer expansion on electrochemical lithium storage.

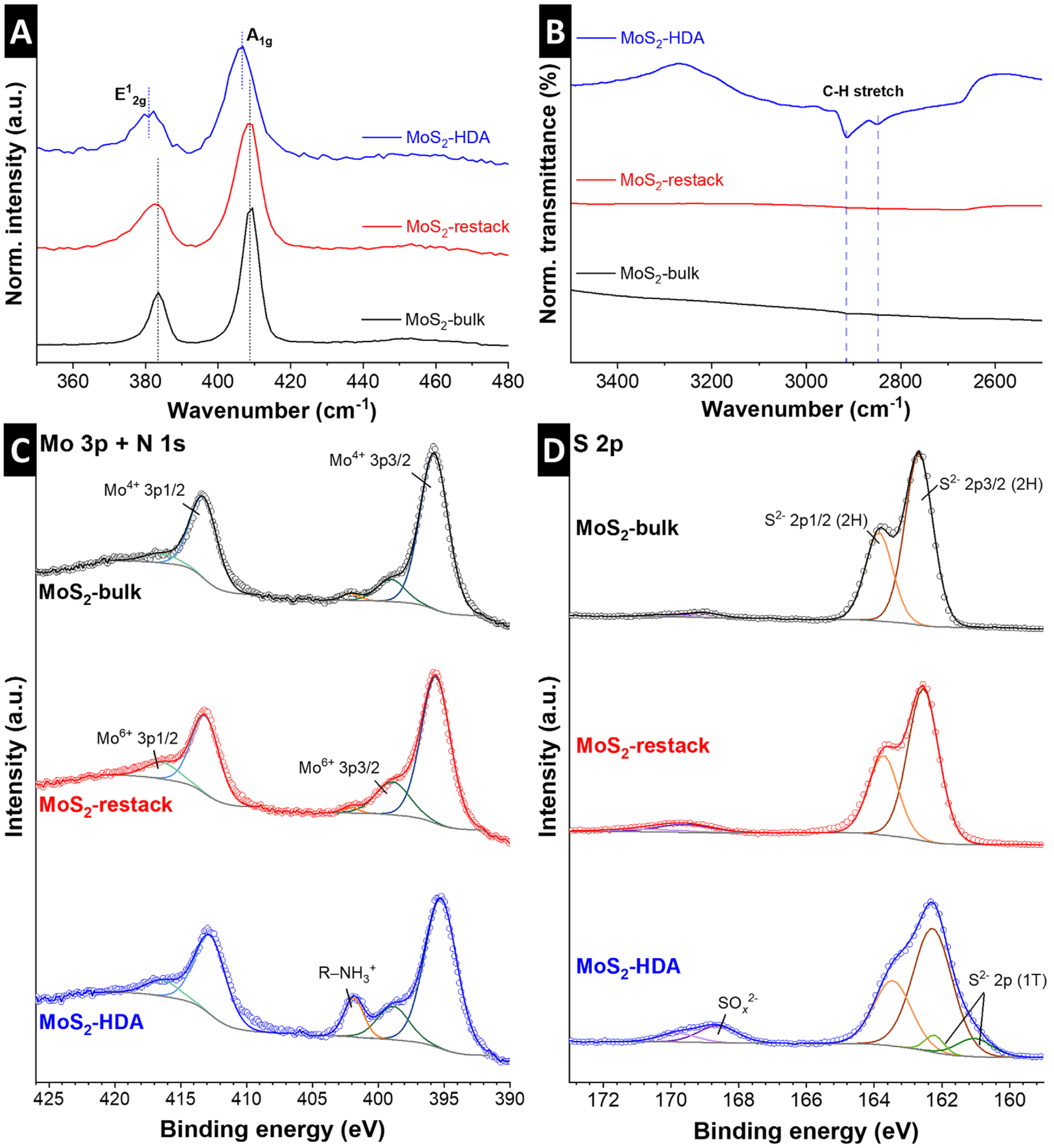

FIGURE 3 | (A) Raman spectra of MoS$_2$-bulk, MoS$_2$-restack, and MoS$_2$-HDA. (B) FTIR spectra, and XPS of the (C) Mo 3p and N 1s and (D) S 2p regions of the MoS$_2$-bulk, MoS$_2$-restack, and MoS$_2$-HDA samples.

3.2 | Electrochemical Characterization of MoS$_2$-Based Materials

The electrochemical investigation of the MoS$_2$-based samples focuses on three major scientific questions. First, we aim to elucidate how the chemical pre-lithiation via butyllithium, exfoliation, and subsequent restacking alters the electrochemical behavior of MoS$_2$-bulk. Second, we analyze the role of interlayer expansion via HDA molecules. Third, we answer how the electrolyte environment influences the intercalation mechanism by comparing a standard, carbonate-based electrolyte with diglyme, which is a solvent known for its propensity to co-intercalation.

The baseline of our investigation is MoS$_2$-bulk in the carbonate-based electrolyte (1ᴍ LiTFSI in ethylene carbonate and dimethyl carbonate, 1:1 by volume). The cyclic voltammogram (CV) shows the typical electrochemical behavior of bulk MoS$_2$, with reversible Li$^+$ (de)intercalation peaks around 1.5–2.1 V (Figure 4A). The CV represents a stabilized electrochemical state after the initial phase evolution, where no further 2H-to-1T phase transition is observed. The phase transition occurs during the initial cycles, as shown in Figure S4A. In this regime, the redox peaks exhibit a significant scan-rate-dependent shift toward lower (reduction) potentials with increasing scan rate, indicating increasing polarization and diffusion-limited kinetics (Figure S5A).

The MoS$_2$-restacked sample shows similar redox features to MoS$_2$-bulk, but with notable differences in intensity and shape. The reduction feature associated with the 2H-to-1T phase transition in the initial cycles (Figure S4B,E) is less pronounced,

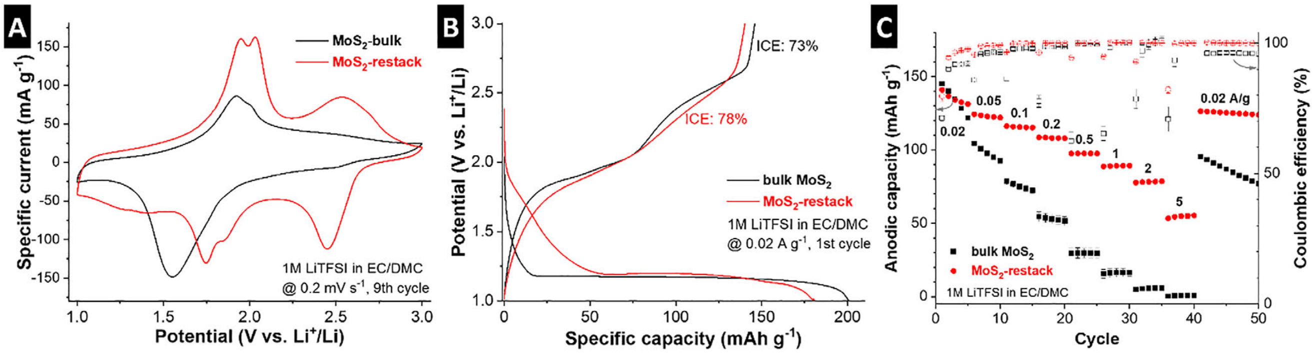

FIGURE 4 | Investigating the influence of chemical pre-lithiation, comparing MoS$_2$-bulk and MoS$_2$-restack electrodes in EC/DMC electrolyte. (A) CV comparison at 0.2 mV s^{-1} (overall nineth cycle). (B) First GCD cycle at 0.02 A g^{-1}. (C) Anodic / delithiation capacity from GCD at varying rates from 0.02 to 5 A g^{-1}. All measurements are carried out in coin cells at 20°C. Error bars indicate standard deviation from 2-3 independent measurements.

which can be attributed to the partial presence of 1T-MoS$_2$ already formed during chemical pre-reduction. In the stabilized CV (Figure 4A), the current response of MoS2-restack is significantly higher, reflected in an increased enclosed CV area, indicating enhanced charge storage. In particular, the redox peaks associated with Li$^+$ (de)intercalation in the range of 1.7–2.1 V are more pronounced compared to pristine MoS2-bulk, and the peak separation between cathodic and anodic processes is reduced. In addition, a second redox peak couple centered around ca. 2.5 V becomes more distinct in MoS$_2$-restack.

In the first galvanostatic charge-discharge (GCD) cycle, the reduction profile of MoS$_2$-bulk is dominated by the 2H-to-1T phase transition plateau, and the initial Coulombic efficiency (ICE) is 73% (Figure 4B). The phase transition is less pronounced for MoS$_2$-restacked in agreement with CVs. Moreover, the MoS$_2$-restacked sample exhibits more sloping regions and a slightly increased ICE of 78%, suggesting that the chemical pre-treatment does not lead to increased parasitic reactions during electrochemical (de)lithiation. Both samples exhibit a comparable maximum anodic/delithiation capacity of 146 (MoS$_2$-bulk) and 140 mAh g^{-1} (MoS$_2$-restacked), corresponding to a reversible storage capacity of 0.84-0.87 Li$^+$ per formula unit of MoS$_2$. Interestingly, the rate capability of MoS$_2$-restacked is strongly improved over MoS$_2$-bulk (Figure 4C). For example, at a high rate of 5 A g^{-1}, the electrode still delivers a reversible capacity of about 55 mAh g^{-1}, while MoS$_2$-bulk exhibits close to 0 capacity at this rate. This suggests that the chemical pre-reduction treatment and its associated partial exfoliation play a major role in enabling high rate electrochemical (de)lithiation of MoS$_2$. Even though both MoS$_2$-bulk and MoS$_2$-restacked exhibit the same BET-surface area, the reduced stacking order and/or partial 1T-phase transition in MoS$_2$-restack likely contribute to the enhanced charge storage kinetics. The presence of partially delaminated layers together with metallic 1T domains may enhance electronic conductivity and facilitate faster Li$^+$ intercalation. This interpretation is further supported by *b*-value analysis of CVs at varying rates, where MoS$_2$-bulk exhibits typical diffusion-limited kinetics and MoS$_2$-restack trends toward surface-limited kinetics (Figure S5). Long-term cycling measurements also confirm the improved electrochemical performance of MoS$_2$-restack (Figure S7A), showing that MoS$_2$-bulk undergoes pronounced capacity fading, retaining only 30% after 200 cycles at 0.1 A g^{-1}, while MoS$_2$-restack exhibits improved stability with a capacity retention of 78%.

Having established the influence of the chemical pre-reduction, the influence of HDA pillaring can be isolated by a comparison of MoS$_2$-restack and MoS$_2$-HDA. The CV comparison in the stabilized state (Figure 5A) shows several distinct differences between the two electrodes. MoS$_2$-HDA exhibits a lower overall current response, with smaller and broader redox features in the range of 1.7–2.1 and 2.5 V compared to MoS$_2$-restack. In addition, the current response of MoS$_2$-HDA becomes more quasi-rectangular, particularly at lower potentials, indicating an increased contribution from pseudocapacitive processes, consistent with previous observation from nanosized, HDA-pillared MoS$_2$ [6]. The initial cycles (Figure S4C) show that the reduction feature associated with the 2H-to-1T phase transition is less pronounced in MoS$_2$-HDA, which is consistent with a faster phase transition during the early cycles.

The observations are confirmed in GCD, where the first reduction of MoS2-HDA also does not show an obvious plateau for 1T formation (Figure 5B). The ICE is reduced compared to the MoS$_2$-restack with 66%. The maximum capacity of MoS$_2$-HDA is reduced to 112 mAh g^{-1}, but this includes the mass contribution of HDA pillars; the measured lithiation capacity translates to 0.78 Li$^+$ per MoS$_2$. The rate behavior of MoS$_2$-HDA is slightly reduced compared to MoS$_2$-restack (Figure 5C), but still significantly improved compared to MoS$_2$-bulk. This trend is consistent with the corresponding *b*-value analysis (Figure S5A–C). Importantly, these results confirm that chemical pre-reduction dominates the rate capability, while interlayer expansion via pillaring does not provide an additional enhancement under these conditions. Instead, the role of interlayer expansion becomes more evident in controlling the intercalation mechanism and structural stability, as discussed below.

Finally, we probe the influence of the electrolyte solvent on the lithium intercalation properties of the MoS$_2$-based materials. Besides the standard, carbonate-based electrolyte system (EC/DMC), we probe the mechanism in an ether-based electrolyte, namely diglyme (2G), which is known for its strong solvating power and tendency to co-intercalate in sulfide-based electrode materials. A comparison of MoS$_2$-bulk in both

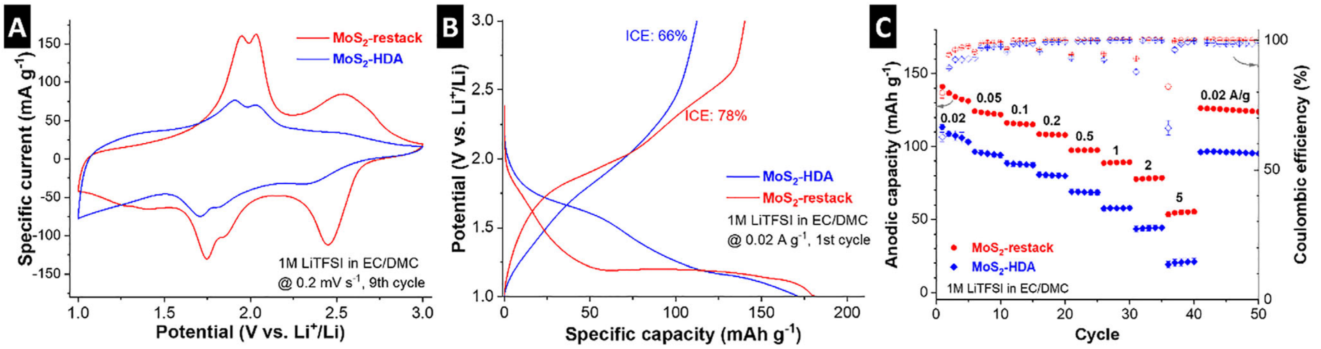

FIGURE 5 | Investigating the influence of interlayer expansion by HDA-pillaring, comparing MoS$_2$-restack and MoS$_2$-HDA electrodes in EC/DMC electrolyte. (A) CV comparison at 0.2 mV s^{-1} (overall nineth cycle). (B) First GCD cycle at 0.02 A g^{-1}. (C) Anodic / delithiation capacity from GCD at varying rates from 0.02 to 5 A g^{-1}. All measurements are carried out in coin cells at 20°C. Error bars indicate standard deviation from 2-3 independent measurements.

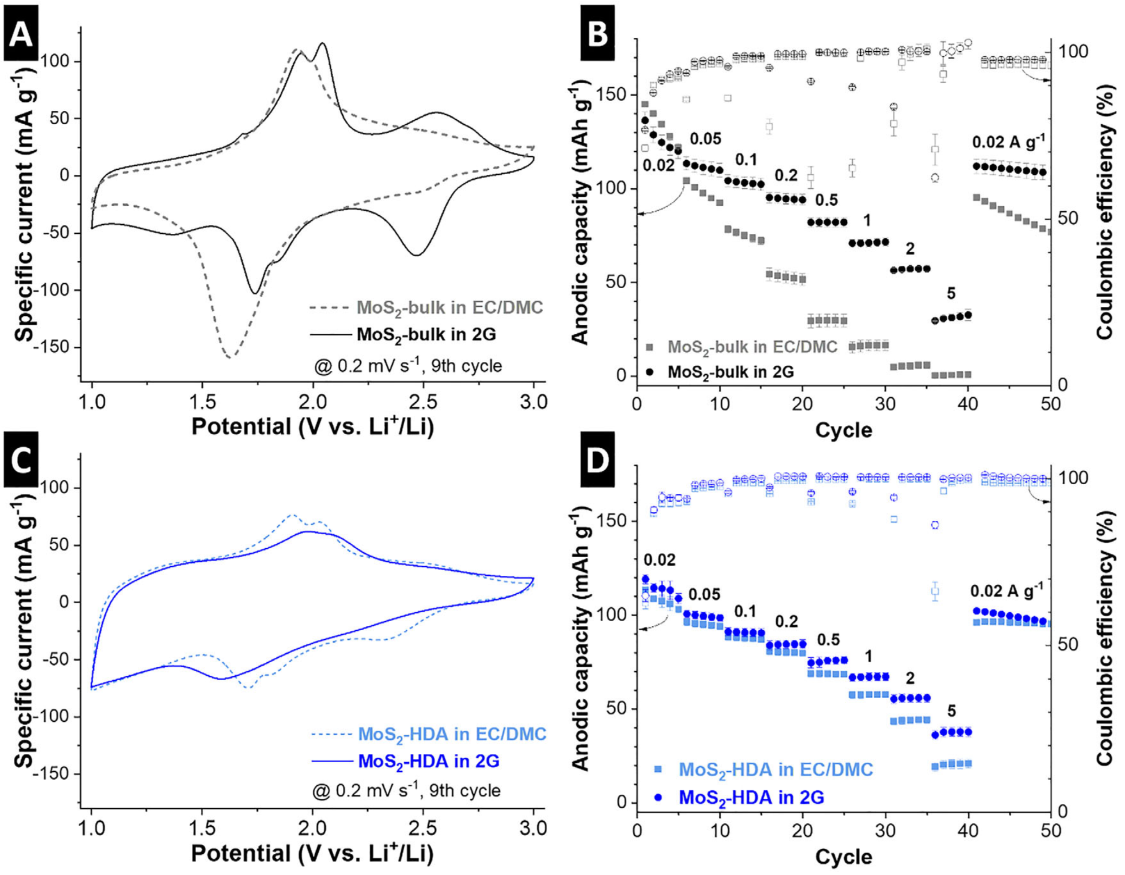

FIGURE 6 | Investigating the influence of electrolyte solvent comparing MoS$_2$-bulk and MoS$_2$-HDA in EC/DMC and 2G electrolytes. (A) CV comparison of MoS$_2$-bulk at 0.2 mV s^{-1} (overall nineth cycle). (B) Anodic / delithiation capacity of MoS$_2$-bulk from GCD at varying rates from 0.02 to 5 A g^{-1}. (C) CV comparison of MoS$_2$-HDA at 0.2 mV s^{-1} (overall nineth cycle). (D) Anodic / delithiation capacity of MoS$_2$-HDA from GCD at varying rates from 0.02 to 5 A g^{-1}. All measurements are carried out in coin cells at 20°C. Error bars indicate standard deviation from 2-3 independent measurements.

electrolytes by CVs shows similar features, but the magnitude of the peaks around 2.5 V is slightly increased in 2G, while the reduction peak of the 1T-phase transformation is slightly suppressed (Figure 6A). The first few cycles from CV and GCD in diglyme are further shown in Figure S7. Strikingly, the rate capability of MoS$_2$-bulk is highly improved in 2G compared to EC/DMC. Even at a GCD rate of 5 A g^{-1}, there is still a reversible capacity of up to 33 mAh g^{-1} in 2G electrolyte, compared to practically zero in EC/DMC (Figure 6B). Long-term cycling performance further shows the beneficial effect of the 2G electrolyte over carbonates (Figure S7B), with MoS$_2$-bulk retaining 50% of its initial capacity after 200 cycles at 0.1 A g^{-1}. The improved kinetics are also visible from *b*-value analysis (Figure S5D–F). Given the tendency for solvent co-intercalation in

2G-based electrolytes, these results may indicate a solvent-dependent change of intercalation mechanism and kinetics.

When probing MoS_2-HDA in the two different electrolytes, there are almost no differences in the CV signatures, except a slight broadening of the redox peak features around 1.7–2.1 V in 2G electrolyte (Figure 6C). Moreover, the rate capability in both electrolytes is also much closer than for the MoS_2-bulk electrodes, although a modest advantage of the 2G electrolyte over EC/DMC remains (Figure 6D), consistent with slightly higher *b*-values (Figure S5F). A capacity retention of 64.0% after 200 cycles at 0.1 A g^{-1} is observed (Figure S7B). However, the strongly overlapping CV curves and comparable rate capability do not necessarily suggest an electrolyte-dependent change of intercalation mechanism like in MoS_2-bulk. Overall, the baseline electrochemical characterization indicates a strong performance dependence of the electrochemical Li^+ intercalation reaction from the electrolyte solvent (EC/DMC vs. 2G) in MoS_2-bulk, but to a lesser extent in MoS_2-HDA, with significantly improved rate capability in 2G electrolyte for MoS_2-bulk electrodes. The underlying mechanisms will be investigated in the following section.

3.3 | Analysis of Electrolyte-Dependent Lithium Intercalation Mechanisms

To correlate the distinct electrochemical behavior observed in carbonate- and diglyme-based electrolytes with specific storage mechanisms, both the crystallographic evolution and the macroscopic volume changes of MoS_2-based electrodes are monitored in real time using operando X-ray diffraction (XRD) and electrochemical dilatometry (ECD), respectively. These techniques are complementary and probe structural changes across multiple length scales, providing insight into volume changes during (de)intercalation from the crystallographic level (XRD) to the electrode level (ECD).

MoS_2-bulk and MoS_2-HDA electrodes were investigated using operando XRD during GCD at a specific current of 0.02 A g^{-1} to monitor crystallographic evolution. For MoS_2-bulk (Figure 7A), the initial (002) interlayer spacing of 6.15 Å expands to 6.29 Å during the first cathodic scan, coinciding with the 2H-to-1T phase conversion associated with Li^+ insertion into the MoS_2 layers. Upon subsequent delithiation and relithiation, the (002) reflection exhibits reversible expansion and contraction between approximately 6.30 and 6.37 Å. Excluding the irreversible expansion associated with the phase conversion (6.15 to 6.30 Å), the reversible breathing amplitude of the (002) plane is about 2.7%, indicating a solid-solution intercalation mechanism of desolvated Li^+ after the initial 2H-1T transformation when using the carbonate-based (EC/DMC) electrolyte.

In the ether-based electrolyte (1 M LiTFSI in diglyme, 2G), MoS_2-bulk displays a markedly different structural evolution (Figure 7B). The initial interlayer spacing of 6.13 Å shifts to 6.30 Å during the 2H-to-1T phase conversion at 1.15 V (vs. Li^+/Li). In addition to this signal, a new reflection appears at 14.25 Å (2.25° 2θ using Ag Kα radiation) during the initial reduction plateau, corresponding to an expansion of more than 130% relative to the initial interlayer spacing. Such a drastic expansion is reminiscent of solvent co-intercalation reactions previously reported for TiS_2 electrodes in lithium- and sodium-based ether and propylene carbonate electrolytes [19, 37]. The new reflection is therefore attributed to a fundamental $(001)_{co}$ set of planes corresponding to an expanded MoS_2 interlayer spacing hosting Li^+ together with diglyme solvent molecules. A second-order reflection indexed as $(002)_{co}$ is observed at $2\theta = 4.5°$ (d = 7.12 Å), indicating the formation of an ordered expanded phase. Operando diffractograms with an extended 2θ-range are further shown in Figure S8.

To further support this interpretation at the atomic scale, representative intercalation states were investigated using DFT-based geometry optimization. The optimized interlayer spacing for $Li\text{-}(2G)_2$ complex (model for solvated Li^+ species) intercalated MoS_2 (Figure 7C) corresponds to a lithiated state, in which Li^+ is coordinated by two diglyme molecules, forming a three-dimensional structure that expands the interlayer spacing to 13.55 Å, in good agreement with the experimentally observed spacing of 14.25 Å.

In contrast, to model the delithiated condition while retaining trapped solvent molecules, the Li atom was removed from the $Li\text{-}(2G)_2$ complex, leaving residual 2G molecules confined within the interlayer space. This configuration was used as the initial structure for subsequent geometry optimization. In the absence of Li-centered coordination, the original three-dimensional scaffold is not maintained, and the residual 2G molecules relax into a more flattened, quasi-two-dimensional configuration, resulting in a contracted interlayer spacing of approximately 10.3 Å (Figure 7D).

Simulated XRD patterns derived from these optimized structures reproduce the emergence of a strong $(001)_{co}$ reflection near 13.55 Å and a corresponding $(002)_{co}$ peak near 6.78 Å (Figure 7E), consistent with the operando diffraction features observed during lithiation. Simulated patterns for different coordination configurations ($Li\text{-}(2G)_x$, $x = 1, 2$) are shown in Figure S9.

After delithiation, the disappearance of the ordered expanded phase together with the persistence of a broad feature in XRD corresponding to a d-spacing of approximately 10–13 Å in XRD are consistent with residual solvent molecules remaining within the MoS_2 interlayer space (Figure 7B). These results support the interpretation that ether-based electrolytes enable the formation of a solvation-induced expanded phase in MoS_2-bulk during lithiation, while a partially contracted but still expanded state reflects retained solvent molecules after Li^+ deintercalation.

To corroborate the findings from operando XRD, complementary operando ECD measurements were performed to monitor macroscopic electrode height changes. The MoS_2-bulk electrode cycled in EC/DMC exhibits a height increase of 7.2% during the initial cathodic cycle (Figure 7F), coinciding with the 2H-to-1T phase transformation and Li^+ intercalation. Upon completion of the first lithiation/delithiation cycle, an irreversible height increase of 4.4% relative to the initial electrode thickness remains. In subsequent cycles, the dilatometric changes are limited to reversible variations of up to 2.8%. This moderate electrode breathing is consistent with a mechanism dominated by reversible intercalation of desolvated Li^+ ions and supports the structural evolution observed by operando XRD (Figure 7A).

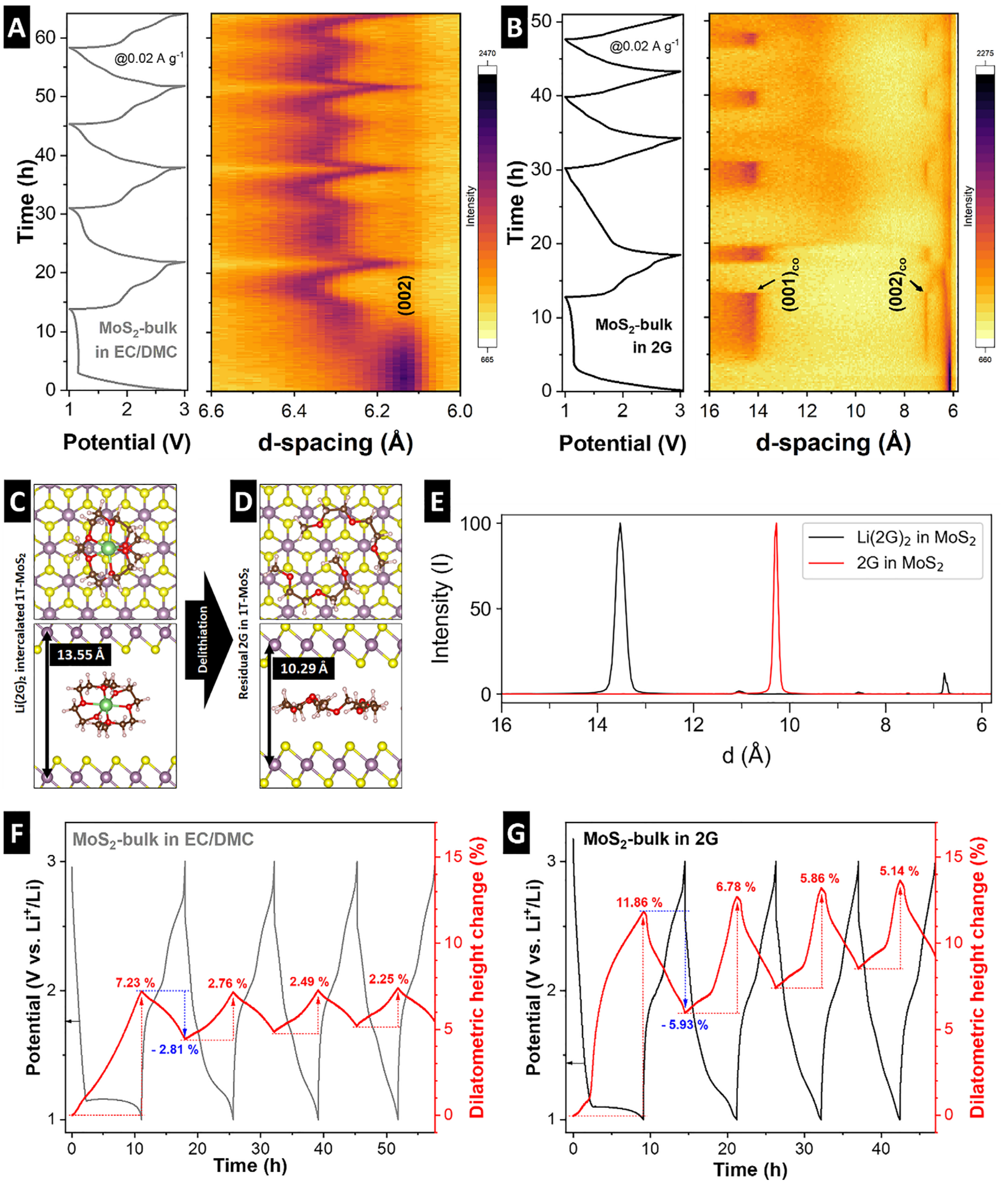

FIGURE 7 | Analysis of the electrolyte-dependent intercalation mechanism in MoS$_2$-bulk. Operando XRD measurements of MoS$_2$-bulk in custom-made coin cells using a transmission geometry and Ag Kα X-ray source with (A) carbonate- and (B) diglyme-based electrolyte for four GCD cycles at 0.02 A g^{-1}. DFT-optimized structures of (C) Li-(2G)$_2$ complex intercalated in MoS$_2$, and (D) 2G molecules intercalated in MoS$_2$ without Li, and (E) corresponding simulated X-ray diffractograms. (F) Electrochemical dilatometry over four GCD cycles at 0.02 A g^{-1} in (F) carbonate- and (G) diglyme-based electrolyte.

In contrast, the use of diglyme electrolyte induces a pronounced expansion of the MoS$_2$-bulk electrode. As shown in Figure 7G, a substantial expansion of 11.9% occurs during the first cathodic scan, followed by a contraction of 5.9%, resulting in an irreversible height increase of approximately 6% after the first cycle, consistent with partial solvent trapping. In subsequent cycles, large reversible height changes of up to 6.8% are observed. These reversible variations significantly exceed the expansion expected for desolvated Li$^+$ intercalation and are consistent with the solvent co-intercalation mechanism identified by operando XRD (Figure 7B). Notably, the electrode retains its expanded height up to approximately 1.7 V during the anodic scan before contracting sharply. The potential at which this contraction occurs correlates with the disappearance of the (001)$_{co}$ and (002)$_{co}$ reflections in operando XRD, linking the macroscopic electrode contraction to the loss of the crystallographic signature of the expanded co-intercalated phase. Together, the operando XRD and ECD results and DFT structure optimization indicate a transition in the lithium storage mechanism in MoS$_2$-bulk from conventional Li$^+$ intercalation to a solvated ion co-intercalation process.

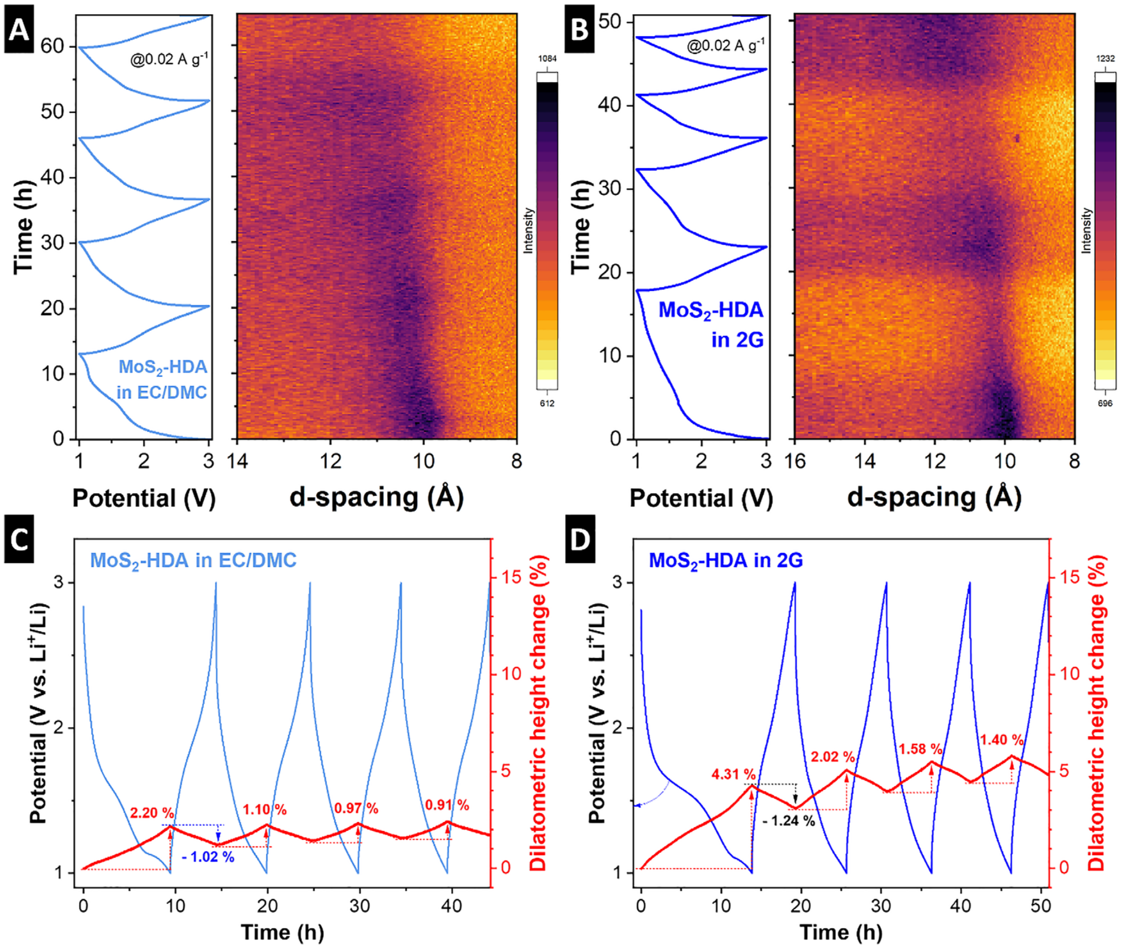

FIGURE 8 | Analysis of the electrolyte-dependent intercalation mechanism in MoS$_2$-HDA. Operando XRD measurements of MoS$_2$-HDA in custom-made coin cells using a transmission geometry and Ag Kα X-ray source with (A) carbonate- and (B) diglyme-based electrolyte for four GCD cycles at 0.02 A g^{-1}. Electrochemical dilatometry over four GCD cycles at 0.02 A g^{-1} in (C) carbonate- and (D) diglyme-based electrolyte.

To evaluate whether interlayer pillaring alters the solvent-dependent intercalation mechanism observed for bulk MoS$_2$, the structural evolution of MoS$_2$-HDA was investigated using operando XRD and ECD. MoS$_2$-HDA in carbonate electrolyte exhibits a moderate expansion of the (002) interlayer spacing from 9.9 to ca. 10.3 Å during the first lithiation (Figure 8A). Upon further lithiation, the *d*-spacing increases to ca. 10.4 Å, corresponding to an overall expansion of approximately 5.1% relative to the initial spacing. In subsequent cycles, the interlayer spacing gradually increases to about 10.6 Å, representing an additional expansion of ~1.9% compared to the end of the first cycle. During lithiation, the intensity of the (002) reflection decreases, indicating decreased stacking order of the expanded layers, which partially recovers upon delithiation. Overall, the moderate lattice breathing and reversible structural evolution are consistent with a solid-solution intercalation mechanism involving Li$^+$ insertion into the expanded MoS$_2$ layers.

When cycled in diglyme electrolyte, MoS$_2$-HDA shows a gradual increase of the interlayer spacing from 9.9 Å to approximately 10.7 Å during the first lithiation/delithiation cycle (Figure 8B). Importantly, no reflections corresponding to a highly ordered solvent co-intercalated phase, such as the 14.25 Å feature observed for bulk MoS$_2$, are detected (see also full range operando diffractograms in Figure S8). Instead, the *d*-spacing evolution closely resembles that observed in the carbonate-based electrolyte. These observations indicate that the confined HDA pillars suppress the formation of a highly expanded solvent co-intercalated phase despite the larger initial interlayer spacing. This finding suggests that interlayer spacing alone is not the decisive factor enabling solvent co-intercalation in bulk-sized MoS$_2$ particles. Rather, we hypothesize that the confined organic pillars inhibit solvent incorporation through steric constraints and possible modifications of the local solvation environment within the interlayer space.

Due to the relatively low intensity of the XRD reflections, complementary operando ECD measurements provide additional insight into the structural evolution of MoS$_2$-HDA during lithium (de)intercalation. In carbonate electrolyte, the MoS$_2$-HDA electrode exhibits very small electrode breathing (Figure 8C), with an initial thickness increase limited to 2.2% and subsequent reversible variations of approximately 1.1% during further cycles. These small height changes make solvent co-intercalation unlikely, in agreement with the operando XRD results. When cycled in diglyme electrolyte (Figure 8D), the MoS$_2$-HDA electrode shows somewhat larger height variations, with an irreversible initial expansion of about 3.1% followed by reversible thickness changes of up to ~2%. Importantly, the large step-like expansion observed for MoS_2-bulk in 2G is absent. Together with the absence of a distinct co-intercalation XRD signature (Figure 8B), the moderate electrode height changes indicate that solvent co-intercalation into MoS_2-HDA is strongly suppressed even in diglyme electrolyte. Overall, these results demonstrate that while ether electrolytes can induce solvated ion co-intercalation in bulk MoS_2, the introduction of confined interlayer pillars could preserve a conventional, desolvated Li^+ intercalation mechanism and suppress excessive volumetric changes during cycling.

4 | Conclusions

In this work, we demonstrate that interlayer engineering concepts previously developed for nanoscale MoS_2 materials can be translated to bulk-sized particles through a top-down pillaring strategy. Chemical pre-reduction of bulk MoS_2 using butyllithium enables exfoliation and subsequent insertion of hexanediammonium (HDA) pillars, resulting in an expanded interlayer spacing while preserving the macroscopic particle morphology and specific surface area of the bulk material. Structural characterization confirms the formation of MoS_2-HDA with an increased interlayer spacing of 0.98 nm and a mixed 2H/1T phase composition arising from the chemical activation step.

Electrochemical analysis reveals that the improved rate capability of the modified MoS_2 materials is primarily associated with the chemical pre-reduction rather than with the interlayer expansion itself. In contrast, the electrolyte environment strongly influences the lithium storage mechanism. While MoS_2-bulk exhibits conventional Li^+ intercalation in carbonate electrolyte, the use of diglyme induces a transition to a solvent co-intercalation mechanism, as evidenced by large interlayer expansion in operando XRD and pronounced electrode swelling in electrochemical dilatometry.

Importantly, the pillared MoS_2-HDA structure suppresses this solvent co-intercalation behavior despite its larger interlayer spacing. Operando XRD and dilatometry show that MoS_2-HDA undergoes only moderate lattice breathing and electrode expansion in both carbonate and diglyme electrolytes, indicating conventional desolvated Li^+ intercalation. These results demonstrate that solvent co-intercalation in layered MoS_2 is mainly governed by the electrolyte solvation rather than by the interlayer spacing alone.

Overall, this study provides mechanistic insight into how interlayer engineering and electrolyte solvation jointly determine the charge storage behavior of MoS_2 electrodes. The results highlight that top-down pillaring of bulk materials offers a viable strategy to control interlayer spacing and limit excessive volume expansion phenomena driven by solvent co-intercalation.

Author Contributions

J.C. conducted materials synthesis, materials characterization, and electrochemical characterization, including electrochemical dilatometry. P.T. contributed to materials synthesis and characterization. F.J. carried out gas sorption analysis. K.N. conducted the DFT calculations. J.K. performed operando X-ray diffraction data acquisition. M.B.D. carried out X-ray photoelectron spectroscopy. C.S., D.L., and S.F. supervised the work. J.C. and S.F. drafted the manuscript, with input from all co-authors.

Acknowledgements

J.C., P.T., J.K., and S.F. acknowledge funding from the German Federal Ministry of Education and Research (BMBF) in the “NanoMatFutur” program (Grant Number 03XP0423) and financial support from the Helmholtz Association. M.B.D. acknowledges financial support from the Alexander von Humboldt Foundation. F.J. and D.L. acknowledge funding from the Carl-Zeiss-Stiftung for the project “RaAlBatt” (P2022-04-046).

Open access funding enabled and organized by Projekt DEAL.

Conflicts of Interest

The authors declare no conflicts of interest.

Data Availability Statement

Experimental data used in this work is made available on the Zenodo repository (https://zenodo.org) under https://doi.org/10.5281/zenodo.20552324.

References

1. R. Bissessur, J. Heising, W. Hirpo, and M. Kanatzidis, “Toward Pillared Layered Metal Sulfides. Intercalation of the Chalcogenide Clusters $Co_6Q_8(PR_3)_6$ (Q = S, Se, and Te and R = Alkyl) into MoS_2,” *Chemistry of Materials* 8 (1996): 318–320.

2. W. M. R. Divigalpitiya, R. F. Frindt, and S. R. Moriuson, “Inclusion Systems of Organic Molecules in Restacked Single-Layer Molybdenum Disulfide,” *Science* 246 (1979): 369–371, https://doi.org/10.1126/science.246.4928.369.

3. H. Dong, Y. Xu, C. Zhang, et al., “MoS_2 Nanosheets With Expanded Interlayer Spacing for Enhanced Sodium Storage,” *Inorganic Chemistry Frontiers* 5 (2018): 3099–3105, https://doi.org/10.1039/C8QI00969D.

4. N. Feng, R. Meng, L. Zu, et al., “A Polymer-Direct-Intercalation Strategy for MoS_2/Carbon-derived Heteroaerogels with Ultrahigh Pseudocapacitance,” *Nature Communications* 10 (2019): 1372, https://doi.org/10.1038/s41467-019-09384-7.

5. J. Choi, K. Nam, Y. T. Malik, et al., “Interlayer Spacing Control of MoS_2 with Covalent Thiol Functionalization: Understanding Structure and Electrochemistry from Experiments and Simulation,” *ACS Nano* 19 (2025): 35425–35437, https://doi.org/10.1021/acsnano.5c07717.

6. J. Choi, H. Moon, and S. Fleischmann, “Simultaneous Control of Crystallite Size and Interlayer Spacing of MoS_2 to Achieve Pseudocapacitive Lithium Intercalation,” *Electrochimica Acta* 476 (2024): 143774, https://doi.org/10.1016/j.electacta.2024.143774.

7. J. B. Cook, H.-S. Kim, T. C. Lin, C.-H. Lai, B. Dunn, and S. H. Tolbert, “Pseudocapacitive Charge Storage in Thick Composite MoS_2 Nanocrystal-Based Electrodes,” *Advanced Energy Materials* 7 (2017): 1601283, https://doi.org/10.1002/aenm.201601283.

8. J. B. Cook, H.-S. Kim, Y. Yan, et al., “Mesoporous MoS_2 as a Transition Metal Dichalcogenide Exhibiting Pseudocapacitive Li and Na-Ion Charge Storage,” *Advanced Energy Materials* 6 (2016): 1501937, https://doi.org/10.1002/aenm.201501937.

9. V. Augustyn and Y. Gogotsi, “2D Materials With Nanoconfined Fluids for Electrochemical Energy Storage,” *Joule* 1 (2017): 443–452.

10. M. Armand and J.-M. Tarascon, “Building Better Batteries,” *Nature* 451 (2008): 652–657, https://doi.org/10.1038/451652a.

11. L. Xu, W. Ma, L. Wang, C. Xu, H. Kuang, and N. A. Kotov, “Nanoparticle Assemblies: Dimensional Transformation of Nanomaterials and Scalability,” *Chemical Society Reviews* 42 (2013): 3114–3126, https://doi.org/10.1039/c3cs35460a.

12. E. Pomerantseva, F. Bonaccorso, X. Feng, Y. Cui, and Y. Gogotsi, “Energy Storage: the Future Enabled by Nanomaterials,” *Science* 366 (2019): aan8285, https://doi.org/10.1126/science.aan8285.

13. M. Acerce, D. Voiry, and M. Chhowalla, “Metallic 1T Phase MoS_2 Nanosheets as Supercapacitor Electrode Materials,” *Nature Nanotechnology* 10 (2015): 313–318, https://doi.org/10.1038/nnano.2015.40.

14. H. D. Yoo, Y. Li, Y. Liang, Y. Lan, F. Wang, and Y. Yao, “Intercalation Pseudocapacitance of Exfoliated Molybdenum Disulfide for Ultrafast Energy Storage,” *ChemNanoMat* 2 (2016): 688–691.

15. A. Ambrosi, Z. Sofer, and M. Pumera, “Lithium Intercalation Compound Dramatically Influences the Electrochemical Properties of Exfoliated MoS_2,” *Small* 11 (2015): 605–612, https://doi.org/10.1002/smll.201400401.

16. H. Guo, M. Elmanzalawy, P. Sivakumar, and S. Fleischmann, “Unifying Electrolyte Formulation and Electrode Nanoconfinement Design to Enable New Ion–solvent Cointercalation Chemistries,” *Energy & Environmental Science* 17 (2024): 2100–2116, https://doi.org/10.1039/D3EE04350A.

17. G. A. Ferrero, G. Åvall, K. Janßen, et al., “Solvent Co-Intercalation Reactions for Batteries and beyond,” *Chemical Reviews* 125 (2025): 3401–3439, https://doi.org/10.1021/acs.chemrev.4c00805.

18. Y. Sun, G. Åvall, S.-H. Wu, et al., “Solvent Co-Intercalation in Layered Cathode Active Materials for Sodium-ion Batteries,” *Nature Materials* 24 (2025): 1441–1449, https://doi.org/10.1038/s41563-025-02287-7.

19. G. Alvarez Ferrero, G. Åvall, K. A. Mazzio, et al., “Co-Intercalation Batteries (CoIBs): Role of TiS_2 as Electrode for Storing Solvated Na Ions,” *Advanced Energy Materials* 12 (2022): 2202377, https://doi.org/10.1002/aenm.202202377.

20. F. Neese, “The ORCA Program System,” *WIREs Computational Molecular Science* 2 (2012): 73–78, https://doi.org/10.1002/wcms.81.

21. A. D. Becke, “Density-Functional Thermochemistry. III. The Role of Exact Exchange,” *The Journal of Chemical Physics* 98 (1993): 5648–5652, https://doi.org/10.1063/1.464913.

22. P. J. Stephens, F. J. Devlin, C. F. Chabalowski, and M. J. Frisch, “Ab Initio Calculation of Vibrational Absorption and Circular Dichroism Spectra Using Density Functional Force Fields,” *The Journal of Physical Chemistry* 98 (1994): 11623–11627, https://doi.org/10.1021/j100096a001.

23. M. J. van Setten, et al., “The PSEUDODOJO: Training and Grading a 85 Element Optimized Norm-Conserving Pseudopotential Table,” *Computer Physics Communications* 226 (2018): 39–54.

24. J. P. Perdew, K. Burke, and M. Ernzerhof, “Generalized Gradient Approximation Made Simple,” *Physical Review Letters* 77 (1996): 3865–3868, https://doi.org/10.1103/PhysRevLett.77.3865.

25. S. Grimme, J. Antony, S. Ehrlich, and H. Krieg, “A Consistent and Accurate Ab Initio Parametrization of Density Functional Dispersion Correction (DFT-D) for the 94 Elements H-Pu,” *The Journal of Chemical Physics* 132 (2010): 154104, https://doi.org/10.1063/1.3382344.

26. K. Momma and F. Izumi, “VESTA 3 for Three-dimensional Visualization of Crystal, Volumetric and Morphology Data,” *Journal of Applied Crystallography* 44 (2011): 1272–1276, https://doi.org/10.1107/S0021889811038970.

27. Z. Li, I. Sami, J. Yang, J. Li, R. V. Kumar, and M. Chhowalla, “Lithiated Metallic Molybdenum Disulfide Nanosheets for High-Performance Lithium–Sulfur Batteries,” *Nature Energy* 8 (2023): 84–93, https://doi.org/10.1038/s41560-022-01175-7.

28. P. Joensen, R. F. Frindt, and S. R. Morrison, “Single-layer MoS_2,” *Materials Research Bulletin* 21 (1986): 457–461, https://doi.org/10.1016/0025-5408(86)90011-5.

29. M. Thommes, K. Kaneko, A. V. Neimark, et al., “Physisorption of Gases, with Special Reference to the Evaluation of Surface Area and Pore Size Distribution (IUPAC Technical Report),” *Pure and Applied Chemistry* 87 (2015): 1051–1069, https://doi.org/10.1515/pac-2014-1117.

30. W. Zhu and A. R. Kamali, “Thermal Oxidation of MoS_2 into Defective Crystalline MoO_3 with Enhanced Li-ion Storage Kinetics,” *Journal of Alloys and Compounds* 968 (2023): 171823, https://doi.org/10.1016/j.jallcom.2023.171823.

31. J. Rahmatinejad and Z. Ye, “Advanced MoS_2 Nanocomposites for Post-Lithium-Ion Batteries,” *Chemical Engineering Journal* 500 (2024): 156872, https://doi.org/10.1016/j.cej.2024.156872.

32. H. Li, Q. Zhang, C. C. R. Yap, et al., “From Bulk to Monolayer MoS_2: Evolution of Raman Scattering,” *Advanced Functional Materials* 22 (2012): 1385–1390, https://doi.org/10.1002/adfm.201102111.

33. S. Jimenez Sandoval, D. Yang, R. F. Frindt, and J. C. Irwin, “Raman Study and Lattice Dynamics of Single Molecular Layers of MoS_2,” *Physical Review B* 44 (1991): 3955–3962, https://doi.org/10.1103/PhysRevB.44.3955.

34. A. Molina-Sánchez, K. Hummer, and L. Wirtz, “Vibrational and Optical Properties of MoS_2: From Monolayer to Bulk,” *Surface Science Reports* 70 (2015): 554–586, https://doi.org/10.1016/j.surfrep.2015.10.001.

35. J. Karol, C. O. Ogolla, M. Sotoudeh, et al., “Nanoconfinement Geometry of Pillared V_2O_5 Determines Electrochemical Ion Intercalation Mechanisms, Storage Sites, and Diffusion Pathways,” *ACS Nano* 19 (2025): 26904–26919, https://doi.org/10.1021/acsnano.5c08169.

36. T. S. Moore and T. F. Winmill, “CLXXVII.—The State of Amines in Aqueous Solution,” *Journal of the Chemical Society* 101 (1912): 1635–1676, https://doi.org/10.1039/CT9120101635.

37. R. G. Houdeville, A. P. Black, A. Ponrouch, M. R. Palacín, and F. Fauth, “Operando Synchrotron X-ray Diffraction Studies on TiS_2: the Effect of Propylene Carbonate on Reduction Mechanism,” *Journal of The Electrochemical Society* 168 (2021): 030514, https://doi.org/10.1149/1945-7111/abe983.

Supporting Information

Additional supporting information can be found online in the Supporting Information section.

Supporting File: adfm76503-sup-0001-SuppMat.pdf.